A CFD-PBM-PMLM Integrated Model for the Gas–Solid Flow Fields in Fluidized Bed Polymerization Reactors

Wei-Cheng Yan, Zheng-Hong Luo, Ying-Hua Lu, and Xiao-Dong Chen
Dept. of Chemical and Biochemical Engineering, College of Chemistry and Chemical Engineering, Xiamen University, Xiamen 361005, China

DOI 10.1002/aic.12705
Published online July 19, 2011 in Wiley Online Library (wileyonlinelibrary.com).

Although the use of computational fluid dynamics (CFD) model coupled with population balance (CFD-PBM) is becoming a common approach for simulating gas–solid flows in polydisperse fluidized bed polymerization reactors, a number of issues still remain. One major issue is the absence of modeling the growth of a single polymeric particle. In this work a polymeric multilayer model (PMLM) was applied to describe the growth of a single particle under the intraparticle transfer limitations. The PMLM was solved together with a PBM (i.e. PBM-PMLM) to predict the dynamic evolution of particle size distribution (PSD). In addition, a CFD model based on the Eulerian-Eulerian two-fluid model, coupled with PBM-PMLM (CFD-PBM-PMLM), has been implemented to describe the gas–solid flow field in fluidized bed polymerization reactors. The CFD-PBM-PMLM model has been validated by comparing simulation results with some classical experimental data. Five cases including fluid dynamics coupled purely continuous PSD, pure particle growth, pure particle aggregation, pure particle breakage, and flow dynamics coupled with all the above factors were carried out to examine the model. The results showed that the CFD-PBM-PMLM model describes well the behavior of the gas–solid flow fields in polydisperse fluidized bed polymerization reactors. The results also showed that the intraparticle mass transfer limitation is an important factor in affecting the reactor flow fields. © 2011 American Institute of Chemical Engineers *AIChE J*, 58: 1717–1732, 2012
Keywords: fluidized bed polymerization reactor, computational fluid dynamics, population balance model, polymeric multilayer model

Introduction

Fluidized-bed reactor (FBR) is one of the most popular commercial reactors to produce polyolefin. FBR is well known as an excellent reactor for its simple construction, excellent heat and mass transfer capabilities and efficient mixing of reacting species.[1] In a fluidized-bed olefin polymerization reactor, small catalyst particles (e.g., 20–80 μm) are introduced at a point above the gas distributor. When these catalyst particles are exposed to the gas stream containing the monomer, polymerization occurs. At the early stage of polymerization, the catalyst particles are fragmentized into a large number of smaller particles, which are quickly encapsulated by the newly formed polymer and grow continuously, reaching a size typically of 200–3000 μm. Because of the distribution in polymer particle sizes, segregation occurs and the fully grown polymer particles migrate to the bottom where they are removed from the reactor. Meanwhile, the small particles and fresh catalyst particles tend to migrate to the upper space of reactor and continue to react with monomer.[2–5] Therefore, the reaction system is considered as a gas–solid system and the solid phase can be characterized by particle size distribution (PSD). The gas phase consists of monomer and hydrogen, and the solid phase consists of polymer and/or catalyst particles. Moreover, the PSD can be directly related to particle kinetics, i.e., single particle growth due to polymerization, particle aggregation, and breakage dynamics as shown in Figure 1.[6,7] On the other hand, different length scales, i.e., multiscale, are involved in the process in polydisperse FBRs (see Figure 2). One can see that the detailed modeling of such a reactor is a highly complex task involving reactor design, complex multiphase flow, interphase mass transfer, particle-particle and particle-reactor interactions, intraparticle transfer, and nanoscale phenomena including the chemistry and kinetics of the active sites of the catalyst and the crystallization of the polymer.[8,9] To operate FBR more effectively, it is important to obtain a fundamental understanding of the gas–solid flow behaviors in these FBRs. Because of these reasons, computational fluid dynamics (CFD) is becoming more and more important as a valuable engineering tool to predict flows in FBRs at industrial scales.[10–12] It is well known that CFD is an emerging technique and holds great potential in providing detailed information of the flow field in reactors.[13–15]

In general, two different categories of CFD methods are used to simulate gas–solid flow fields in FBRs, namely the Lagrangian and the Eulerian methods.[10–12] Using the Lagrangian method, the motion of many individual particles is calculated separately. Because of the high numerical effort to calculate the motion of a large number of particles, the

Correspondence concerning this article should be addressed to Z.-H. Luo at luozh@xmu.edu.cn.

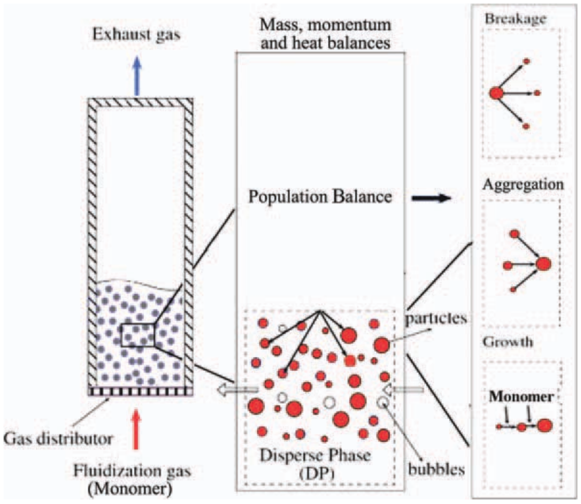

Figure 1. The evolution of PSD in the fluidized-bed olefin polymerization reactor.

[Color figure can be viewed in the online issue, which is available at wileyonlinelibrary.com.]

applicability of this method is restricted to low number densities of the particles. The Eulerian method, on the other hand, considers fully interpenetration of continual subjects hence using continuity and momentum equations. This method needs a comparatively less numerical effort. Considerable attention has been devoted in recent years to the application of CFD to gas–solid FBRs.[10–17] A comprehensive review has been published on these CFD models applied to FBRs.[18] Most authors have used the Eulerian method. To achieve closure, a granular temperature model has usually been introduced. When turbulent flow of the gas phase is assumed, a k-ε model is also incorporated. Following the above description, recently, a CFD model has been described to model the gas–solid flows in fluidized bed polymerization reactors.[19] The entire flow behaviors in FBRs, such as the solid holdup distributions, the bubble behaviors and the solid velocity vectors, were obtained. As a whole, these CFD models can provide reasonably quantitative agreement with the limited experimental findings.[10–20] These previous CFD calculations for gas–solid flows are carried out under only cold-flow conditions with the assumption that the solid phase is monodispersed, whereas it is well known that in many applications, the solid phase is characterized by a PSD.[19–27]

Recently, more attention[28–36] was paid to the understanding of polydisperse reactors/fluidized bed polymerization reactors. Many publications have been published on the PSD in polydisperse fluidized bed polymerization reactors, using particle balance equation (PBE).[2,5–8,37–47] Correspondingly, some hybrid CFD models have been put forward, to describe gas–solid flow fields in reactors, as well as the particle PBE for PSD, namely the CFD-PBM coupled models.[30,33–36,48–53] Notably, Fan et al.[33–36] suggested CFD-PBM coupled models to simulate polydisperse gas–solid FBRs. The quadrature method of moments (QMOM) and direct quadrature method of moments (DQMOM) were used to solve the PBE, and they were implemented in a multifluid model to simulate polydisperse gas–solid FBRs. In the works by Fan et al.,[33–36] QMOM or DQMOM, chemical reaction engineering model, and CFD were combined to investigate roles of intrinsic kinetics and the PSD of catalyst in a gas–solid FBR, wherein polymer PSD and flow field were also predicted. However, several other features (e.g., heat and mass transfer, aggregation and breakage, etc.) were not considered. In particular, the single particle growth effect was not mentioned. More recently, the corresponding author's team also developed a CFD-PBE coupled model to describe gas–solid two-phase flows in polydisperse fluidized bed propylene polymerization reactors.[54] The entire temperature fields in FBRs were modelled. This model has been incorporated the kinetics theory of granular flow, the PBE and the heat exchange coefficient equation based on the Eulerian-Eulerian two-fluid model. In addition, the QMOM is used to solve the PBE and to realize the combination of the CFD model and the PBE. Yet, the single particle growth was still not considered. In addition, the effect of solid holdup was also not mentioned. In practice, it is well known that there are spatial distributions of monomer and temperature in the polymer particles in gas–solid olefin polymerization, which are directly linked to intraparticle mass and heat transfer.[9,55–57] These distributions can influence the polymerization rate and product properties including polymer PSD.[55,56] Therefore, these distributions and intraparticle mass and heat transfer are important for a fundamental modeling, which can influence the simulation results. To study intraparticle mass and heat transfer, material and energy balance equations for single particle growth have to be solved. Namely, the single particle model must be coupled into the CFD-PBM coupled model. To the best of our knowledge, there is so far no open literature regarding the application of "CFD-PBM coupled single particle model" in modeling the flow field in FBR for olefin polymerization.

Up to now, a number of single particle growth models have been proposed for the solid-catalyzed olefin polymerization.[57–66] Among them, four models, namely, the solid core model,[58] the polymeric flow model,[59] the multigrain model,[60,61] and polymeric multigrain model[62,63] have been widely used. The polymeric multilayer model (PMLM) is a versatile model that can also be used to simulate olefin polymerization.[57,64–66] In the previous work at Xiamen University,[38,55] the PMLM was once incorporated into a PBM (a PBE-PMLM coupled model) to predict the PSD in propylene polymerization reactors. Although the PBE-PMLM coupled model can be used to predict PSD of polyolefin produced in reactors including FBR, whilst considering intraparticle mass and heat transfer limitations, a full-picture of the process needs to be used to describe the flow behaviors in reactors.

In this work, a CFD-PBM-PMLM integrated model for the gas–solid flow in fluidized bed propylene polymerization reactor is developed for giving a fuller picture of the

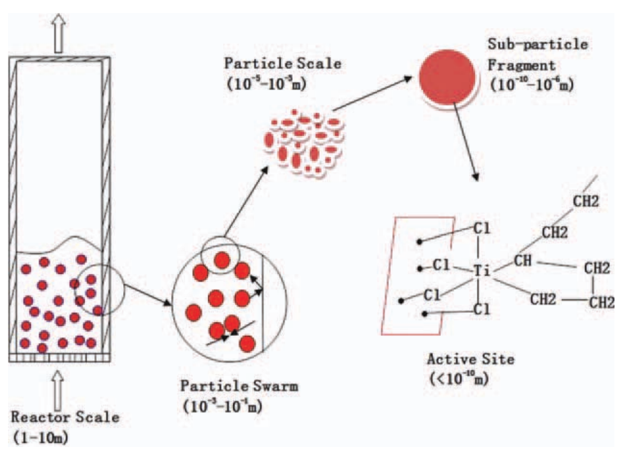

Figure 2. The multiscale phenomenon in the fluidized-bed olefin polymerization reactor.

[Color figure can be viewed in the online issue, which is available at wileyonlinelibrary.com.]

process. Based on the Eulerian-Eulerian two-fluid model, the model incorporates the kinetics theory of granular flow, the PBE embedded with the particle kinetics and the PMLM describing the single particle growth rate under intraparticle transfer limitations. Both the PMLM and PBE are solved using MATLAB 6.5 and the CFD model is solved using the commercial CFD code FLUENT 6.3.26. The interlink between FLUENT and MATLAB is exploited to integrate the different models in a single computational platform in which the essential combination of PMLM, PBE, and CFD model is performed. To the best of our knowledge, this is the first attempt that aims at realizing the combination of all these models in the fluidized bed polymerization reactor. As mentioned in the abstract, five test cases are designed to evaluate the model. Furthermore, the model is then used to investigate the effects of intraparticle transfer limitations on the flow field in the reactor.

The CFD-PBM-PMLM Integrated Model

As described above, a CFD-PBM-PMLM integrated model based on the Eulerian approach was used to describe the gas–solid two-phase flow in fluidized bed polymerization reactor. The intraparticle transfer limitations were considered via the PMLM, and the aggregation and breakage of polymer particles were considered via the PBM. Furthermore, the PMLM was solved together with the PBM to implement the coupling of single particle growth model and PBE, namely, the PBE-PMLM coupled model. In addition, the QMOM was used to solve the PBE-PMLM coupled model and implement the combination of the CFD model and the PBE-PMLM coupled model, namely, the CFD-PBM-PMLM integrated model, which illustrates the physical mechanism of the gas–solid flow field in fluidized bed polymerization reactors (see Figure 3).

In what follows, the general governing equations for the CFD model are first presented. Then, the PMLM, PBM, and QMOM are described respectively. Finally, the implementation of the PMLM and the PBM in the CFD model is presented.

The CFD model

The CFD model is an extension of the two-fluid model for gas–solid flows.[34,67] In this CFD model, the gas and solid phases are treated as interpenetrating continua in an Eulerian framework. The gas phase is considered as the primary phase, whereas the solid phases are considered as secondary or dispersed phases. Each solid phase is characterized by a specific diameter, density and other associated properties. Correspondingly, the governing equations are summarized as follows.[34,54,67–70]

Eulerian-Eulerian Two Fluid Equations. The continuity equations for phase q ($q = g$ for gas, s for solid phases respectively) can be written as

$$\frac{\partial}{\partial t}(\alpha_g\rho_g) + \nabla\cdot(\alpha_g\rho_g\vec{v}_g) = -\dot{m}_{gs}, \quad (1)$$

and

$$\frac{\partial}{\partial t}(\alpha_s\rho_s) + \nabla\cdot(\alpha_s\rho_s\vec{v}_s) = \dot{m}_{gs}, \quad (2)$$

The mass transfer from the gas phase to solid phase can be calculated as

$$\dot{m}_{gs} = \tfrac{1}{2}\pi\rho_s G_{m_2}. \quad (3)$$

The momentum balance equations for gas and solid phases can be expressed as:

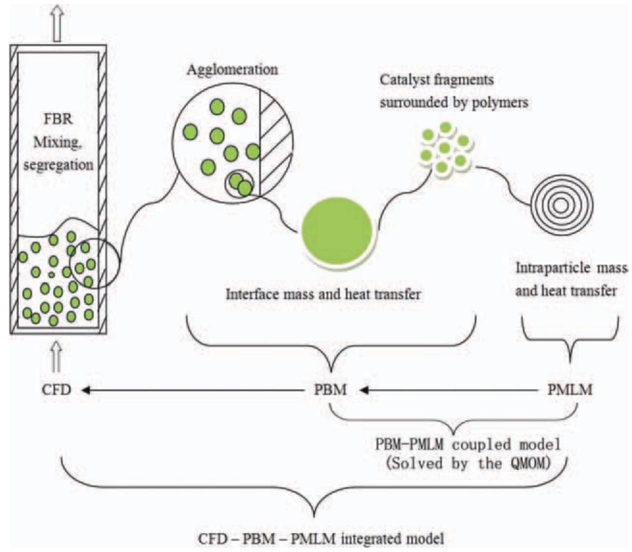

Figure 3. The physical mechanism of the gas–solid flow field in fluidized bed polymerization reactors.

[Color figure can be viewed in the online issue, which is available at wileyonlinelibrary.com.]

$$\frac{\partial}{\partial t}(\alpha_g\rho_g\vec{v}_g) + \nabla\cdot(\alpha_g\rho_g\vec{v}_g\cdot\vec{v}_g) = -\alpha_g\nabla p + \nabla\cdot\bar{\bar{\tau}}_g + K_{gs}(\vec{v}_s - \vec{v}_g) - \dot{m}_{gs}\vec{v}_g + \alpha_g\rho_g g. \quad (4)$$

$$\bar{\bar{\tau}}_g = \alpha_g\mu_g(\nabla\cdot\vec{v}_g + \nabla\cdot\vec{v}_g^{\,T}). \quad (5)$$

$$\frac{\partial}{\partial t}(\alpha_s\rho_s\vec{v}_s) + \nabla\cdot(\alpha_s\rho_s\vec{v}_s\cdot\vec{v}_s) = -\alpha_s\nabla p - \nabla p_s + \nabla\cdot\bar{\bar{\tau}}_s + K_{gs}(\vec{v}_q - \vec{v}_s) + \dot{m}_{gs}\vec{v}_s + \alpha_s\rho_s g. \quad (6)$$

$$\bar{\bar{\tau}}_s = \alpha_s\mu_s(\nabla\cdot\vec{v}_s + \nabla\cdot\vec{v}_s^{\,T}) + \alpha_s\left(\lambda_s - \frac{2}{3}\mu_s\right)\nabla\cdot\vec{v}_s\cdot\bar{\bar{I}}. \quad (7)$$

Kinetics Theory of Granular Flow (KTGF). The two-fluid model requires constitutive equations to describe the rheology of the solid phase. When the particle motion is dominated by collision interaction, the concepts from fluid kinetics theory can be introduced to describe the effective stresses in the solid phase resulting from particle streaming collisional contribution. These constitutive relationships for the solid-phase stress based on the kinetic theory concepts were derived by Lun et al.[68] They are also used in this work.

$$p_s = \alpha_s\rho_s\Theta_s[1 + 2g_0\alpha_s(1+e_s)]. \quad (8)$$

$$\lambda_s = \frac{4}{3}\alpha_s^2\rho_s d_s g_0(1+e_s)\sqrt{\frac{\Theta_s}{\pi}}. \quad (9)$$

where,

$$g_0 = \frac{1}{1 - \left(\alpha_s/\alpha_{s,\max}\right)^{1/3}}. \quad (10)$$

$$\Theta_s = \frac{1}{3}\overline{v_s' v_s'}. \quad (11)$$

Besides Eqs. 8–11, the transport equation for the temperature in a granular/particle that is essential in this work is according to Ding and Gidaspow's model:[69]

$$\frac{3}{2}\left[\frac{\partial}{\partial t}(\rho_s\alpha_s\Theta_s) + \nabla\cdot(\rho_s\alpha_s\vec{v}_s\Theta_s)\right] = (-p_s\bar{\bar{I}} + \bar{\bar{\tau}}_s):\nabla\vec{v}_s + \nabla\cdot(k_{\Theta_s}\nabla\Theta_s) - \gamma_{\Theta_s} + \phi_{gs}, \quad (12)$$

where, the diffusion coefficient for granular energy, k_{Θ_s}, is given by Syamlal et al.:[67]

$$k_{\Theta_s} = \frac{15\rho_s d_s \alpha_s \sqrt{\pi\Theta_s}}{4(41-33\eta)}\left[1+\frac{12}{5}\eta^2(4\eta-3)\alpha_s g_0 + \frac{16}{15\pi}(41-33\eta)\eta\alpha_s g_0\right], \quad (13)$$

with

$$\eta = \frac{1}{2}(1+e_s). \quad (14)$$

The collision dissipation of energy, γ_{Θ_s}, is modeled using the correlation by Lun et al.:[68]

$$\gamma_{\Theta_s} = \frac{12(1-e_s^2)g_0}{d_s\sqrt{\pi}}\rho_s\alpha_s^2\Theta_s^{1.5}. \quad (15)$$

$$\phi_{gs} = -3K_{gs}\Theta_s. \quad (16)$$

In this study, the granular energy was assumed at steady state and dissipated locally. The convection and diffusion were also neglected. Accordingly, Eq. 12, which is a complete granular temperature transport equation, can be rewritten to an algebraic equation and the simplified equation is as follows:

$$0 = (-p_s\bar{\bar{I}} + \bar{\bar{\tau_s}}) : \nabla\vec{v}_s - \gamma_{\Theta_s} - 3K_{gs}\Theta_s. \quad (17)$$

According to our previous works,[19,54,71] the solid phase dynamic viscosity is expressed as follows:

$$\mu_s = \mu_{s,col} + \mu_{s,kin} + \mu_{s,fr}. \quad (18)$$

where,

$$\mu_{s,col} = \frac{4}{5}\alpha_s\rho_s d_s g_o(1+e_s)\sqrt{\frac{\Theta_s}{\pi}}. \quad (19)$$

$$\mu_{s,kin} = \frac{10 d_s\rho_s\sqrt{\Theta_s\pi}}{96\alpha_s(1+e_s)g_0}\left[1+\frac{4}{5}(1+e_s)\alpha_s g_0\right]^2. \quad (20)$$

and

$$\mu_{s,fr} = \frac{p_s\sin\theta}{2\sqrt{I_{2D}}}. \quad (21)$$

Drag force Model. The transfer of forces between the gas and solid phases was described by an empirical drag law proposed by Gidaspow et al.[23] Correspondingly, the main equations are listed as the following:

$$\text{at } \alpha_g > 0.8, \quad K_{sg} = \frac{3}{4}C_D\frac{\alpha_S\alpha_g\rho_g\left|\vec{v}_s - \vec{v}_g\right|}{d_s}\alpha_g^{-2.65}, \quad (22)$$

where,

$$C_D = \frac{24}{\alpha_g Re_s}\left[1+\left(\frac{3}{20}\alpha_g Re_s\right)^{0.687}\right]. \quad (23)$$

$$Re_s = \frac{\rho_g d_s\left|\vec{v}_s - \vec{v}_g\right|}{\mu_g}, \quad (24)$$

$$\text{at } \alpha_g \le 0.8, \; K_{sg} = 150\frac{\alpha_s(1-\alpha_g)\mu_g}{\alpha_g d_s^2} + \frac{7}{4}\frac{\alpha_s\rho_g\left|\vec{v}_s - \vec{v}_g\right|}{d_s} \quad (25)$$

Turbulent Model. A standard k-ε model is used to solve the transport equations for k and ε.[72,73] The k-ε model is usually written into two equations:

$$\nabla\cdot(\rho_m k\vec{v_m}) = \nabla\cdot\left(\frac{\mu_{t,m}}{\sigma_\varepsilon}\nabla k\right) + G_{k,m} - \rho_m\varepsilon, \quad (26)$$

$$\nabla\cdot(\rho_m\varepsilon\vec{v_m}) = \nabla\cdot\left(\frac{\mu_{t,m}}{\sigma_\varepsilon}\nabla\varepsilon\right) + \frac{\varepsilon}{k}(C_{1\varepsilon}G_{k,m} - C_{2\varepsilon}\rho_m\varepsilon). \quad (27)$$

With the assumption of excellent mixing in the reactor these lead to:

$$\rho_m = \sum_{i=1}^{N}\alpha_i\rho_i, \quad (28)$$

$$\vec{v_m} = \frac{\sum_{i=1}^{N}\alpha_i\rho_i\vec{v_m}}{\sum_{i=1}^{N}\alpha_i\rho_i}, \quad (29)$$

and

$$\mu_{t,m} = \rho_m C_\mu\frac{k^2}{\varepsilon}, \quad (30)$$

and the above have been assumed to hold in the cases simulated in this study.

The population balance model and QMOM

The population balance concept, first presented by Hulburt and Katz,[49] is a well-established method in computing the size distribution of the dispersed phase and in accounting for the breakage and aggregation effects in multiphase flows. In our previous work,[54] the PBM based on Hulburt and Katz's idea was applied to describe the PSD. In this work, the PBM is based on the basic theory of Hulburt and Katz with a few modifications. The modifications are to do with the consideration of intraparticle transfer limitations due to the addition of PMLM. Correspondingly, the main equations are summarized as follows.[34–36,49,54,74,75]

General Population Balance Equation. Based on Ref. 49, a general form of the population balance equation is given as follows:

$$\frac{\partial n(L;x,t)}{\partial t} + \nabla\cdot[\vec{u}n(L;x,t)] = -\frac{\partial}{\partial L}[G(L)n(L;x,t)] + B_{ag}(L;x,t) - D_{ag}(L;x,t) + B_{br}(L;x,t) - D_{br}(L;x,t). \quad (31)$$

where, $n(L;x,t)$ is the number density function with particle diameter (L) as the internal coordinate, $G(L)n(L;x,t)$ is the particle flux due to molecular growth rate, $B_{ag}(L;x,t)$ and $D_{ag}(L;x,t)$ are the birth and death rates of particles diameter (L) due to aggregation, respectively, and $B_{br}(L;x,t)$ and $D_{br}(L;x,t)$ are the birth and death rate of particles diameter (L) due to breakage, respectively. In Eq. 31, the first term on the left hand is the transient term, the second term is the convective term, and the terms on the right hand are the source term describing particle growth, aggregation, and breakage dynamics, respectively.

QMOM. The QMOM is used to track the particle size evolution by solving a system of differential equations in lower order moments. The moments of the PSD are defined as follows:

$$m_{kk}(x,t) = \int_0^\infty n(L;x,t)L^{kk}dL \qquad kk = 0,1,\cdots,2N-1. \quad (32)$$

where N is the order of the quadrature approximation, kk is the specified number of moments and some moments have special meanings, such as m_0, m_1, m_2, and m_3, which are related to the total number, length, area, and volume of solid particles per unit volume of mixture suspension, respectively. In addition, the sauter mean diameter (L_{32}) is usually recognized as the mean particle size and is defined according to Eq. (33).

$$L_{32} = \frac{m_3}{m_2} \tag{33}$$

Applying the moment transformation into Eq. 31 results in:

$$\frac{\partial m_{kk}}{\partial t} + \nabla \cdot (\vec{u} m_{kk}) = -\int_0^\infty k L^{kk-1} G(L) n(L;x,t) dL + \bar{B}_{ag}(L;x,t) - \bar{D}_{ag}(L;x,t) + \bar{B}_{br}(L;x,t) - \bar{D}_{br}(L;x,t). \tag{34}$$

where, $B_{ag}(L;x,t), D_{ag}(L;x,t), B_{br}(L;x,t),$ and $D_{br}(L;x,t)$ are given by:

$$B_{ag,kk} = \frac{1}{2}\int_0^\infty n(\lambda;x,t) \int_0^\infty \beta(\lambda,L)(\lambda^3 + L^3)^{kk/3} n(\lambda;x,t) dL d\lambda. \tag{35}$$

$$D_{ag,kk} = \int_0^\infty L^{kk} n(L;x,t) \int_0^\infty \beta(\lambda,L) n(\lambda;x,t) dL d\lambda. \tag{36}$$

$$B_{br,kk} = \int_0^\infty L^{kk} \int_0^\infty a(\lambda) b(L|\lambda) n(\lambda;x,t) dL d\lambda. \tag{37}$$

$$D_{br,kk} = \int_0^\infty L^{kk} a(L) n(L;x,t) dL. \tag{38}$$

where $\beta(\lambda, L)$ is the aggregation kernel, $a(L)$ is the breakage kernel, and $b(L|\lambda)$ is the fragment distribution function that contains the information of fragments produced by a breakage event.

The QMOM uses a quadrature approximation as follows:

$$m_{kk} = \int_0^\infty n(L;x,t) L^{kk} dL \approx \sum_{i=1}^{N} w_i L_i^{kk}. \tag{39}$$

where the weights (w_i) and abscissas (L_i) are determined through the product-difference (PD) algorithm from the lower-order moments.[76] By applying the quadrature approximation, the transformed moment PBE can be written as:

$$\frac{\partial m_{kk}}{\partial t} + \nabla \cdot (\vec{u} m_{kk}) = k \sum_{i=1}^{N} L_i^{kk-1} G(L_i) w_i + \frac{1}{2} \sum_{i=1}^{N} w_i \sum_{j=1}^{N} w_j (L_i^3 + L_j^3)^{kk/3} \beta(L_i, L_j) - \sum_{i=1}^{N} L_i^{kk} w_i \sum_{j=1}^{N} w_j \beta(L_i L_j) + \sum_{i=1}^{N} w_i \int_0^\infty L_{kk} a(L_i) b(L|L_i) dL - \sum_{i=1}^{N} L_i^{kk} w_i a(L_i). \tag{40}$$

Namely, applying the QMOM method, $B_{ag,kk}$, $D_{ag,kk}$, $B_{br,kk}$, and $D_{br,kk}$ can be described via the following equations:[2,77]

$$B_{ag,kk} = \frac{1}{2} \sum_{i=1}^{N} w_i \sum_{j=4}^{N} w_j (L_i^3 + L_j^3)^{kk/3} a(L_i, L_j), \tag{41}$$

$$D_{ag,kk} = \sum_{i=1}^{N} L_i^{kk} w_i \sum_{i=1}^{N} w_j a(L_i, L_j), \tag{42}$$

$$B_{br,kk} = \sum_{i=1}^{N} w_i \int_0^\infty L_{kk} g(L_i) \beta(L) dL, \tag{43}$$

$$D_{br,kk} = \sum_{i=1}^{N} L_i^{kk} w_i g(L_i). \tag{44}$$

Therefore, the PBE in Eq. 40 is solvable via the QMOM by following the evolution of w_i and L_i, as well as m_{kk}. The moments are related to the weights and abscissas by Eq. 39.

The local value of particle growth rate $G(L)$ is related to the single particle growth model, which can be defined as:

$$G(L_i) = \frac{d(L_i)}{dt}. \tag{45}$$

In this study, the intraparticle transfer limitations are considered via the addition of PMLM into the PBM. Namely, $G(L)$ is obtained via the PMLM. In the following subsection, the PMLM and the computation produce of $G(L)$ based on the PMLM are described.

PMLM and the solution of G(L)

The PMLM is used to solve the single particle growth rate along with the effects of intraparticle transfer limitations. In our previous work,[38] the PMLM has been used to consider the effects of intraparticle transfer limitations in a slurry loop reactor.[38] Although the current reactor is a gas–solid reactor, the PMLM may still be used due to the general nature of the model.[57,64–66] The main equations for the PMLM are summarized as follows.[38,57,64–66]

Polymerization Kinetics. To describe the kinetics of propylene polymerization on a Ziegler-Natta catalyst, a simple kinetics model is used, which is the same as that used in our previous work.[38] The polymerization kinetics scheme comprises of a series of elementary reactions, namely, site activation, propagation, site deactivation, chain transformation, and chain transfer reactions. Here, the main elementary reactions and corresponding kinetics equations are listed.

$$\text{Propagation rate}: \ R_p = k_p C^* \rho_{cat} M \tag{46}$$

where the rate constant (k_p) is:

$$k_p = k_p^0 \exp(-E_A / \mathrm{R_{gas}} T). \tag{47}$$

Because propylene is consumed by the propagation reaction, the polymerization rate is given by Eq. 46 in this study.

Catalyst deactivation can be described as a first-order reaction:

$$C^* = C_0^* \exp(-k_d t) \tag{48}$$

with

$$k_d = k_d^0 \exp(-E_D / \mathrm{R_{gas}} T). \tag{49}$$

PMLM. To simulate single polymer particle growth, the PMLM (Figure 4) is applied.[38,57,64–66] Moreover, the reaction system in a FBR is driven by a gaseous monomer with a high fluidization rate, and there is no monomer concentration gradient in film layer around particle during polymerization. In addition, high thermal diffusivity of gas and turbulence in the FBR make external heat transfer resistance (if present) negligible. Accordingly, the external boundary transfer resistance of the polymer particle is considered to be very small and it is assumed reasonable to neglect in the single particle model.[9,57] Accordingly, the main equations are summarized below.[34–36,49,54,74,75]

The PMLM accounting for the intraparticle mass and heat transfer limitations and the deactivation of active sites

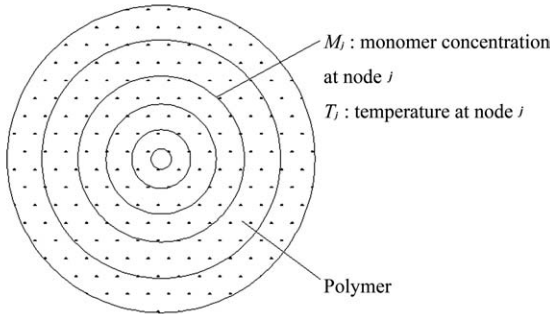

Figure 4. Schematic representation of the PMLM.

comprises the following differential equations and boundary conditions.

$$\frac{\partial M(r,t)}{\partial t} = \frac{D_e}{r^2}\frac{\partial}{\partial r}\left(r^2\frac{\partial M}{\partial r}\right) - R_p. \tag{50}$$

$$\rho_p C_P \frac{\partial T(r,t)}{\partial t} = \frac{K_e}{r^2}\frac{\partial}{\partial r}\left(r^2\frac{\partial T}{\partial r}\right) - Q_p. \tag{51}$$

where, R_p is described by Eqs. (46)-(49), and Q_p is expressed as follows:

$$Q_p = (-\Delta H_p)R_p. \tag{52}$$

The initial and boundary conditions for solving Eq. (50) are:

$$M(r,0) = 0, \tag{53}$$

$$\frac{\partial M(0,t)}{\partial r} = 0, \tag{54}$$

$$M(R,t) = M_0. \tag{55}$$

and for solving Eq. (51):

$$T(r,0) = T_0, \tag{56}$$

$$\frac{\partial T(0,t)}{\partial r} = 0. \tag{57}$$

$$T(R,t) = T_0, \tag{58}$$

The volume and boundary position of each layer must be updated after a predetermined time interval, Δt. The monomer concentrations in the previous time step are used for this purpose, and the discretized equations are expressed as:

$$V_j^{(0)} = \frac{4}{3}\pi\left[(r_{j+1}^{(0)})^3 - (r_j^{(0)})^3\right]. \tag{59}$$

$$V_j^{(i+1)} = V_j^{(i)}\left[\frac{k_p C_j^{*(i)} M_j M_m \Delta t \rho_{cat}}{\rho_p} + 1\right]. \tag{60}$$

$$r_{j+1}^{(i+1)} = \left[\frac{3}{4\pi}V_j^{(i+1)} + (r_j^{(i+1)})^3\right]^{1/3}. \tag{61}$$

In these equations, the superscripts indicate time and the subscripts indicate the radial position; for example, $V_j^{(i)}$ and $r_j^{(i)}$ are the volume of layer j and the radial position of the layer during the growth, the polymeric particle in the ith time interval, respectively. For updating the volume, the concentration of active sites that depend on the volume of layers in layer j in the ith time interval, $C_j^{*(i)}$, is expressed as:

$$C_j^{*(i+1)} = C_j^{*(i)} V_j^i / V_j^{(i+1)}. \tag{62}$$

The effect of deactivation on $C_j^{*(i)}$ is described by Eqs. (48)-(49).

The Solution of G(L) *and the PBM-PMLM Coupled Model.* Based on the PMLM (Eqs. 46–62), one can obtain the particle growth rate, $G(L)$. When one substitutes the obtained $G(L)$ into Eq. (34), it means that the PMLM is solved together with a PBM to obtain the dynamic evolution of PSD. Therefore, the coupling of PMLM and PBM is implemented. The detailed solution process of $G(L)$ is as follows.

First, we obtain the radial profiles of the monomer concentration, the temperature, the concentrations of active sites, and the polymerization rate in the polymeric particle based on the PMLM. Next, we obtain the polymerization rate of each layer in the polymeric particle according to Eq. 46. Accordingly, the total particle polymerization rate can be given as follows:[38]

$$G = \sum_{j=1}^{n}\left(R_{p_j}^{(i)}\left(V_j^{(i)} C_j^{*(i)} \Big/ \sum_{j=1}^{n}(V_j^{(i)} C_j^{*(i)})\right)\right). \tag{63}$$

where n is the total number of layers. Simultaneously, the polymeric particle diameter ($L = 2 \times r_n^i$) can be obtained according to Eqs. 59–61. Finally, the least square method is used to fit the particle growth rate with L as the independent variable and G as the dependent variable. Therefore, the PMLM is incorporated into the PBE to predict the effects of intraparticle transfer limitations on PSD.

The integrated CFD-PBM-PMLM model

Particles in the fluidized bed polymerization reactor have a size distribution due to particle growth, aggregation, and breakage. In two-phase CFD simulations, generally a two-fluid model is applied with particles of a constant diameter instead of different sizes in the dispersed phase by ignoring the single particle growth due to polymerization. However, if the PSD is wide or multimodal, this approach is more likely to fail.[78] The coupling of the CFD model and the PBM-PMLM coupled model, i.e., the CFD-PBM-PMLM integrated model, can overcome this drawback.

Figure 5 shows the schematic of CFD-PBM-PMLM integrated model developed in this study. The solid volume fraction and particle velocity calculated from the Navier-Stokes transport equations by CFD are used to solve the PBM, since they are related to the particle growth, aggregation, and breakage. In addition, the particle growth rate calculated from the intraparticle mass and heat transfer equations by the PMLM is also used to solve the PBM, since it is related to the intraparticle transfer limitations. Once the PBE is solved, moments of PSD can be utilized to calculate the sauter diameter to further modify the interphase force in the two-fluid model and the particle diameter in the PMLM, and hence update the information of solid volume fraction, particle velocity and particle growth rate for PBM. Thus, an integration of CFD, PBM and PMLM is achieved. Both CFD and PBM-PMLM coupled model can improve each other in the integrated model.

Simulation Conditions and CFD Modeling Method

Simulated object

We have done a fundamental CFD study of the gas–solid flow field in a two-dimensional (2D) fluidized bed

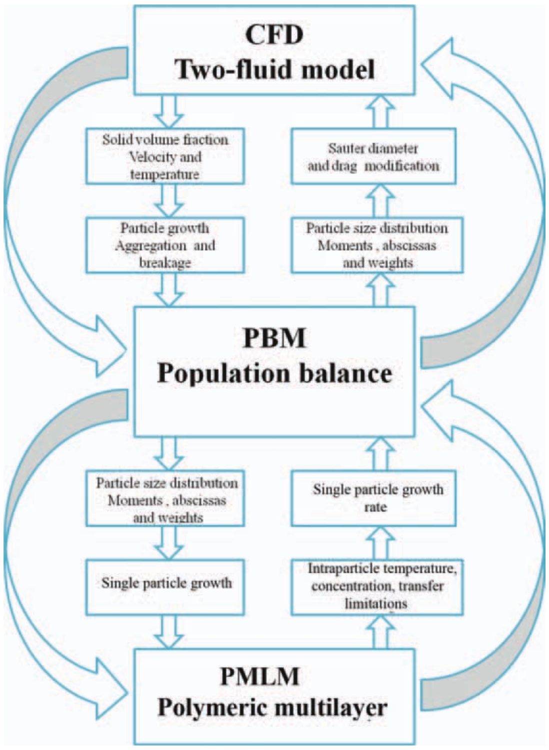

Figure 5. Integrated model in the CFD-PBM-PMLM integrated model.

[Color figure can be viewed in the online issue, which is available at wileyonlinelibrary.com.]

polymerization reactor assuming that the solid phase is monodispersed at cold-flow conditions.[71] In addition, many model parameters were also examined in our previous study.[71] Herein, the 2D FBR reported in our previous work[71] is still selected as our object. The selected reactor has an inner diameter of 0.33 m, a height of 0.90 m, and an initial bed height of 0.2 m, which is shown in Figure 6.

Model parameters

It is well known that the simulated results depend on the range of parameter values presented in Eqs. 1–63. Most of parameters are directly linked to the properties of the gas and solid phases in the reactor. In addition, in our previous studies,[38,54,71] most of model parameters were investigated and optimized, although our previous studies assumed that the solid phase was monodispersed at cold-flow conditions[38,71] or ignored the intraparticle transfer limitations.[54] In this study, a set of values of these parameters reported in our previous studies[38,54,71] have been selected and are listed in Tables 1 and 2. Unless otherwise noted, the parameters used for the next simulations are those listed in Tables 1 and 2.

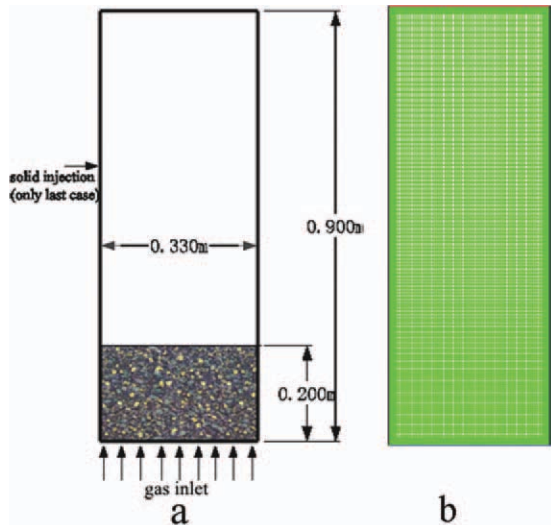

Figure 6. The FBR: configurations: (a) reactor configuration, (b) CFD grid.

[Color figure can be viewed in the online issue, which is available at wileyonlinelibrary.com.]

CFD modeling

The 2D simulations based on the CFD-PBM-PMLM integrated model were performed with the industrial CFD code FLUENT 6.3.26 (Ansys) in double precision mode. The phase coupled SIMPLE algorithm was used to couple pressure and velocity. A commercial grid-generation tool, GAMBIT 2.3.16 (Ansys, Canonsburg, PA) was used to generate the 2D geometries and the grids. Grid sensitivity was carried out initially and the results indicated that a total amount of 15,520 cells was adequate to conserve the mass of solid phase in the dynamics model.[71] The equations and source terms of the PMLM and PBM were defined via external user-defined scalars and user-defined functions (UDF). A three-stage calculation was implemented. First, the flow field was simulated without the particle growth, aggregation and breakage process until the fully fluidized flow field reached. Afterward, the intraparticle monomer concentration and temperature distributions were simulated within MATLAB 6.5 to obtain the particle growth rate, which was used to improve the PBM. The PSDs were simulated by the improved PBM within MATLAB 6.5, which was used to improve the CFD model. The above obtained intraparticle monomer concentration and temperature distributions, single particle growth rate, and PSDs data were coupled into the CFD

Table 1. Model Parameters for CFD Model[23,67,68]

Descriptions	Values	Descriptions	Values
Angle of internal friction	30°	Particle density	900 kg m^{-3}
Gas density	21.56 kg m^{-3}	Gas viscosity	1.081×10^{-5} Pa·s
Granular temperature	Algebraic	Restitution coefficient	0.9
Drag law	Gidspow	Granular viscosity	Gidspow
Inlet boundary condition	Velocity inlet	Granular bulk viscosity	Lun et al.
Outlet boundary condition	Pressure outlet	Frictional viscosity	Schaeffer
Turbulent kinetic energy	$6.87 \cdot 10^{-4}$ m^2 s^{-2}	Turbulent dissipation rate	$1.28 \cdot 10^{-4}$ m^2 s^{-3}
Wall boundary condition	No slip for air and free slip for solid phase, the diabatic heat- transfer equation	Initial solid packing	0.6
Operating pressure	$1.40 \cdot 10^6$ Pa	Convergence criteria	$1 \cdot 10^{-3}$
Maximum iterations	50	Time step	$1 \cdot 10^{-3}$ s

Table 2. Model Parameters for PMLM 2-10

Descriptions	Values	Descriptions	Values
C_p	1400 J·kg^{-1} K^{-1}	C_0^*	0.2 mol kg^{-1}
D_e	10^{-10}–10^{-11} m^2 s^{-1}	E_A [J/mol]	5×10^4 J·mol^{-1}
E_D	5×10^4 J·mol^{-1}	K_e	0.12–0.18 W·m^{-1} K^{-1}
k_p^0	1.2×10^4 m^3·mol^{-1} s^{-1}	M_0	9700 mol m^{-3}
T_0	343 K	ΔH_p	85830 J·mol^{-1}
ρ_{cat}	2840 kg m^{-3}	–	–

model by UDFs. Finally, the reaction process was simulated within Fluent by activating the improved PBM/the PBM-PMLM coupled model.[79] In addition, in the above solution, reconstruction of PSD must be employed, and it is automatically accomplished within FLUENT 6.3.26 (Ansys Inc.) (the reconstruction principle can be found in Ref. 80). Furthermore, the simulations were performed in a platform of Intel 2.83 GHz Xeon with 8 GB of RAM.

Results and Discussion

This section comprises three sub-sections, namely, the CFD-PBM-PMLM integrated model testing, identification, and application. The model is preliminarily validated by comparing the predicted results with the classical experimental results. Five cases including fluid dynamics coupled purely bimodal PSD (Case 1), pure particle growth (Case 2), pure particle aggregation (Case 3), pure particle breakage (Case 4), and flow dynamics coupled with all the above factors (Case 5) were designed to identify the suggested model. Finally, the integrated model was used to investigate the influences of intraparticle transfer limitations on the flow fields.

Model testing

Although one of the most crucial steps in the development of fundamental hydrodynamic model is the validation of these models with accurate and detailed experimental data, to obtain the experimental data is, however, very difficult.[81,82] Indeed, up to now, some hydrodynamic data, such as the flow field data in the fluidized bed polymerization reactor, can not be accurately obtained by experiment. Nevertheless, Goldschmidt et al.[82] have obtained some flow field data experimentally in a cold-flow, pseudo 2D laboratory scale FBR with a simple rectangular geometry and well-defined gas inflow conditions. Their experiments were carried out with 1.5- and 2.5-mm coloured glass beads, for which particle–particle and particle–wall collision parameters were accurately known. Therefore, some of their experimental data are used to preliminarily testify the CFD-PBM-PMLM integrated model.

To compare with the experimental data obtained by Goldschmidt et al.,[82] the simulation conditions are as close to the experimental conditions as possible (see Table 3). In addition, the

Table 3. Main Simulation and Experiment Conditions and Results for Model Testing[82]

Particle Property Data Used in Simulation and Experiment		
	Small Particles	Large Particles
Diameter	1.52×10^{-3} m	2.49×10^{-3} m
Density	2523 kg m^{-3}	2526 kg m^{-3}
Collision Parameters for Particle-Particle Collision Data Used in Simulation and Experiment		
Coefficient of normal restitution	0.97	0.97
Coefficient of friction	0.15	0.10
Collision Parameters for Particle-Wall Collision Data Used in Simulation and Experiment		
Coefficient of normal restitution	0.97	0.97
Coefficient of friction	0.15	0.09
FBR Configuration Data Used in Simulation and Experiment		
Bed hight		0.7m
Bed width		0.15 m
Initial Bed height		0.15 m

Comparison Between Simulation and Experiment Data

	Bed Expansion Height of the Large Particles (m)		Bed Expansion Height of the Small Particles (m)	
Time (s)	Simulation	Experiment	Simulation	Experiment
0-10	0.0853	0.0825	0.0975	0.0958
10-20	0.0810	0.0789	0.1225	0.1037
20-30	0.0802	0.0771	0.1308	0.1106
30-40	0.0766	0.0738	0.1338	0.1152
40-50	0.0732	0.0717	0.1387	0.1211
50-60	0.0719	0.0702	0.1444	0.1238

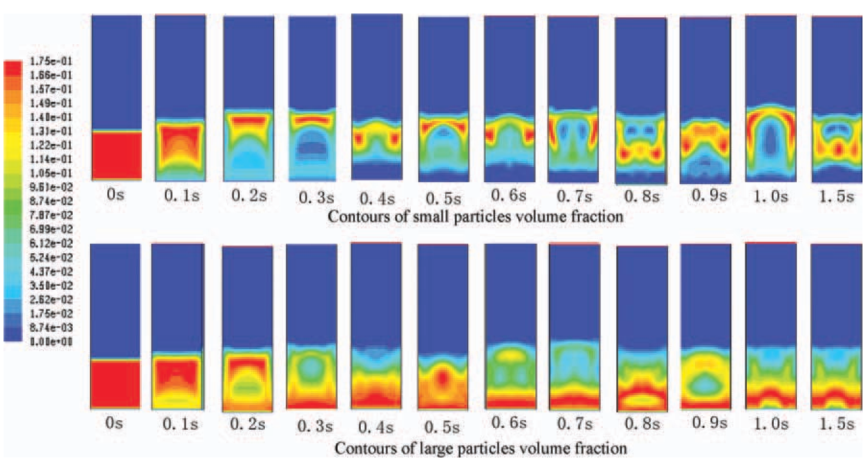

Figure 7. CFD simulation of two kinds of solid diameter mixtures.

[Color figure can be viewed in the online issue, which is available at wileyonlinelibrary.com.]

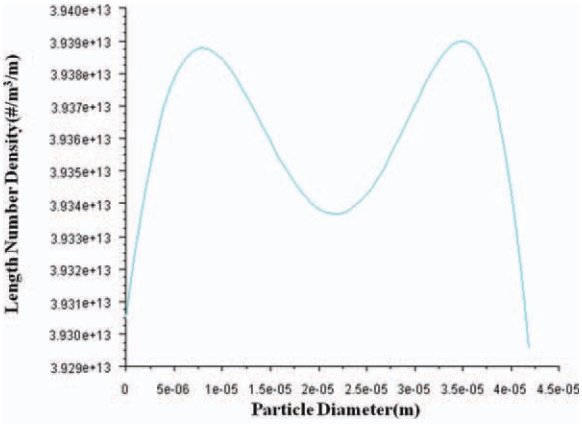

Figure 8. The length number density of initial particles in Case 1.

[Color figure can be viewed in the online issue, which is available at wileyonlinelibrary.com.]

main simulation conditions are listed in Table 3 and the simulation results are given in Figure 7. In addition, the quantitative data of simulation and experiment are also listed in Table 3. From Figure 7, one expects that the mixing of the small and large particles is initially nearly uniform, and then the small particles begin to be fluidized and occupy the top layer of the bed with the continuous addition of gas. Meanwhile, the large particles fall and occupy the bottom layer of the bed. Correspondingly, the separation of the small and large particles occurs and the separation becomes obvious after 0.5 s. It should be pointed out that the simulated inlet-gas velocity is 1.2 $m \cdot s^{-1}$ (as reported/shown in Goldschmidt et al.'s work[82] and Table 3, the minimum fluidization velocities of the small and large particles are 0.78 and 1.2 $m \cdot s^{-1}$, respectively). Accordingly, a small fraction of large particles is also carried to the top layer of the bed along with the generation of bubbles. Figure 7 also shows that most of bubbles are generated and occupy the top layer of the bed. As a whole, the simulation results shown in Figure 7 and Table 3 are in qualitative agreement with the results obtained from Goldschmidt et al.'s experiments.[82]

Model identification

For the five cases described above, besides those listed in Tables 1 and 2, the corresponding simulation conditions are described above. The simulation results and their comparison in the five cases are described as follows step-by-step.

In Case 1, the initial PSD is described in Figure 8 and the simulated solid volume holdup distributions in the reactor are illustrated in Figure 9. From Figure 9, one can obtain the process of bubble formation and development following the flow proceeding in the reactor, whose behavior is basically the same as that in the monodisperse fluidized bed polymerization reactor (please refer to a previous study[71]). However, compared to that with uniform diameter particles in the monodisperse fluidized bed polymerization reactor,[71] fewer bubbles are produced in the reactor in Case 1 as described in Figure 9. In practice, in Case 1, there are different size particles in the reactor and the small particles will fill in the void between the large particles. Accordingly, the voidage in the reactor gets smaller than that with uniform diameter particles, which leads to the less bubbles as shown in Figure 9. Correspondingly, in Case 1, there is less collision of particles and a more uniform fluidization in the reactor as shown in Figure 9. In addition, it is also emphasized herein that the particle growth, particle aggregation and particle breakage are neglected, and only the fact of polydispersity is considered in Case 1 to investigate the effect of PSD on the flow field in the reactor. The results indicate that the addition of

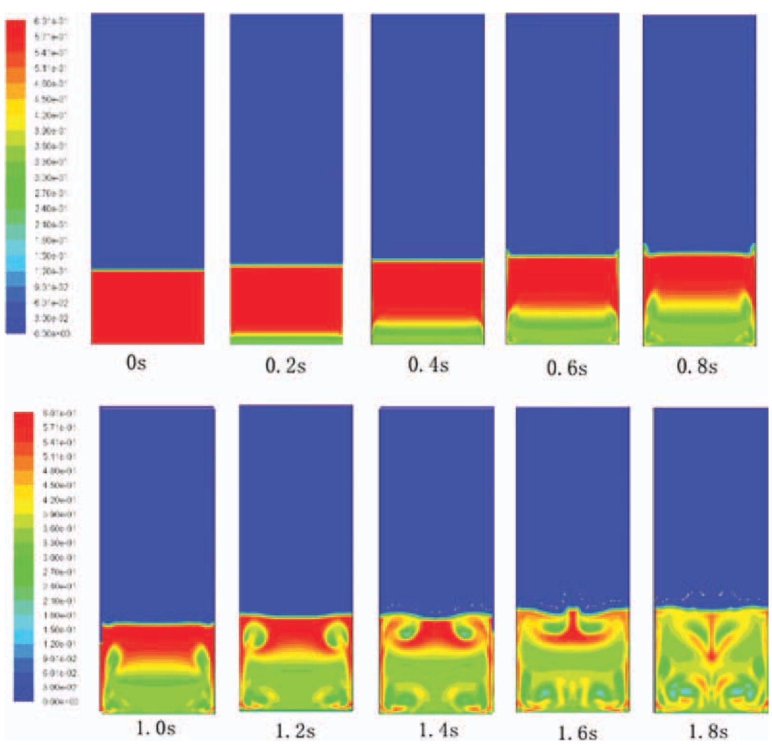

Figure 9. The evolution of solid volume fraction contour in the reactor in Case 1.

[Color figure can be viewed in the online issue, which is available at wileyonlinelibrary.com.]

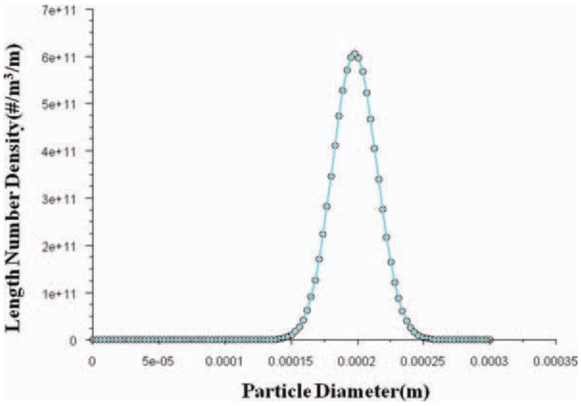

Figure 10. The length number density of initial particles in Cases 2–5.

[Color figure can be viewed in the online issue, which is available at wileyonlinelibrary.com.]

polydispersity is helpful to obtain a more uniform fluidization in the reactor compared to a monodisperse system.

It is well known that the particle growth rate is very slow with its time-step at about 1 h, compared with the time-step (about the order of 1 ms) in simulating the flow field in the reactor. Accordingly, to investigate more effectively if the PBM can simulate the particle growth, the flow dynamics and intraparticle transfer limitations in the reactor are ignored and the particles grow for 3 h at a growth rate described in Eq. (64) in Case 2.

$$G(L_{\rm i}) = \frac{d(L_{\rm i})}{dt} = \frac{R_{\rm p}L_0^3}{3\rho_{\rm s}L_{\rm i}^2}. \tag{64}$$

It means that in Case 2, the flow dynamics, particle aggregation, and particle breakage are neglected and only the particle growth due to polymerization kinetics is considered. In Case 2, the initial PSD is described in Figure 10 and the simulated evolutions of the PSDs within 3 h are illustrated in Figure 11. From Figure 11, one can observe that the particles in the reactor continue to grow with the polymerization proceeding. For instance, the particle average diameter reaches to 1160 μm from the initial 200 μm after 20,000 s. Furthermore, as described in Figure 11, the PSD curve becomes more flat with the growing of particles. In practice, based on Eq. 64, one can predict that the growth rate of smaller particles is faster than that of larger particles. With the polymerization proceeding, the uniformity of particle sizes in the reactor increases and then the PSD gets broader,

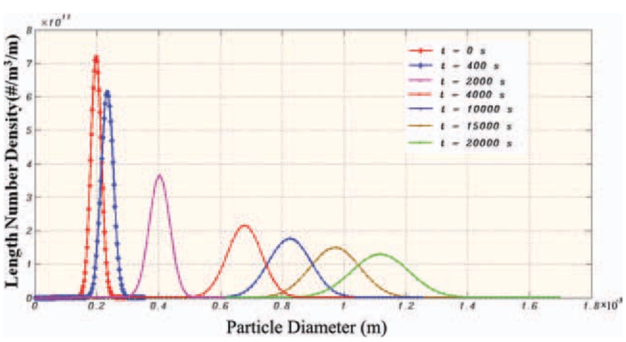

Figure 11. The evolution of PSD with time in Case 2.

[Color figure can be viewed in the online issue, which is available at wileyonlinelibrary.com.]

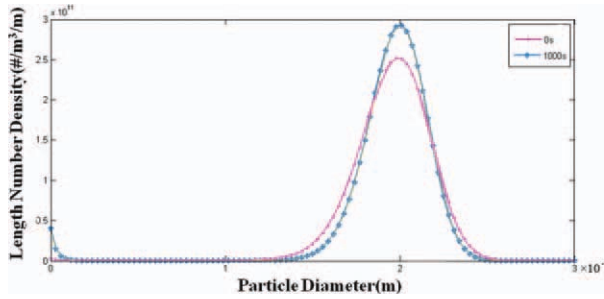

Figure 12. The evolution of PSD with time in Case 3.

[Color figure can be viewed in the online issue, which is available at wileyonlinelibrary.com.]

which is in good agreement with the results obtained via the polymerization kinetics.[5,38,40,43,44,57,77] Therefore, the PBM embedded in the integrated model can be used to describe the particle growth.

Analogously, Cases 3 and 4 are designed to identify the effects of particle aggregation and breakage kernels embedded in the PBM, respectively. Accordingly, in Cases 3–4, pure particle aggregation and breakage are considered with ignoring the flow dynamics, respectively. In addition, in Cases 3 and 4, the initial PSDs are the same (see Figure 10), and the simulated evolutions of the PSDs are illustrated in Figures 12 and 13, respectively. In Case 3, both the particle average diameter and the fraction of large particles increase due to the aggregation of small particles. It leads to the profile of PSD moves toward the upper and right in the reference frame, as described in Figure 12. It indicates that small particles are relatively easier to aggregate than the large particles. In Case 4 (see Figure 13), with polymerization proceeding, the PSDs are basically constant when the breakage is dominant, which is different from our expectation. This may be because the breakage kernel model (see Eqs. 43 and 44) relates to the hydrodynamics equations. However, in Case 4, the flow hydrodynamics is ignored and then the breakage kernel model keeps basically constant. Fan[35] have found that the smaller particles are produced due to the breakage when the kernel model coupled hydrodynamics. Therefore, when Eqs. 43 and 44 are still used to describe the breakage effect, the hydrodynamics must be considered. The hydrodynamics will be considered in the next case (see Case 5).

In Case 5, wherein the flow dynamics is coupled with all above factors (including particle growth, aggregation, and breakage), is designed to simulate the multiscale phenomenon

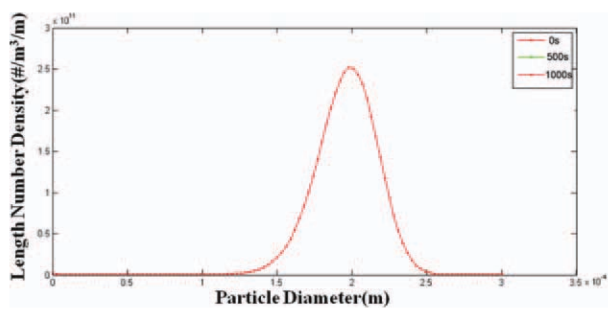

Figure 13. The evolution of PSD with time in Case 4.

[Color figure can be viewed in the online issue, which is available at wileyonlinelibrary.com.]

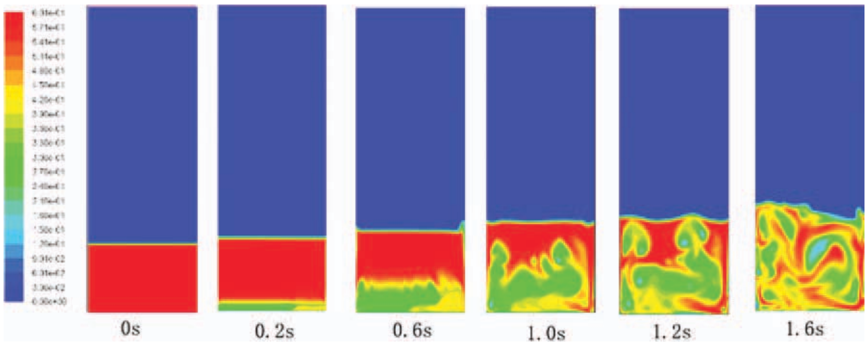

Figure 14. The evolution of solid volume fraction contour in the reactor in Case 5.

[Color figure can be viewed in the online issue, which is available at wileyonlinelibrary.com.]

in the real fluidized bed polymerization reactor. The initial PSD is still the one described in Figure 10, and the simulated results are shown in Figures 14 and 15. Figure 14 gives the contours of solid volume holdup at different times. At 0.2 s in Figure 14, only the particles in the bed bottom become flexible to form an emulsion phase. Accordingly, the bed height rises a little. The bubbles begin to form with further emulsification of the particles at 0.6 s. Simultaneously, as shown at 0.6, 1.0, 1.2, and 1.6 s, the bubbles formed appear to deform due to the interactions between particles and also develop upwards. Comparing Figure 14 with Figure 9, one can see that the development shown in Figure 14 is more complex than that shown in Figure 9. It is expected that there are more complex collisions of the particles since the above three types of particle kinetics factors are considered in Case 5, which leads to a more uneven fluidization in the reactor as shown in Figure 14. On the other hand, the above particle kinetics factors are coupled with the PSD. Therefore, the PSD also changes during the progress of polymerization. Indeed, from Figure 15, it is obvious that the average particle diameter still increases and the profile of PSD becomes flat and moves towards the right in the reference frame as polymerization proceeds, although particle aggregation and breakage all exist at the same time. These changes come from the competition among the particle growth, aggregation and breakage. Furthermore, the altered PSD will influence the flow field, as described in Figures 2 and 5. Therefore, one can say that the flow field in Case 5 is complicated.

From the above simulation results, the results in Case 5 are the closest to the actual flow field in the reactor due to the consideration of PSD and all particle kinetics factors listed in this work. Namely, the simulation results in Case 5 agree best to the reality. Therefore, the model implemented in Case 5 was used to investigate the effects of intraparticle transfer limitations on the flow field in the reactor.

Model application

The coupled CFD-PBM-PMLM model in Case 5 is used for the first time to predict the flow field in the reactor. The comprehensive flow behaviors in the reactor, such as the solid holdup distributions, the bubble behaviors and the solid velocity vectors, were explored. It is noted here that the intraparticle transfer limitations are described through the formulation of the transfer coefficients.[55,60–65]

The Effect of Effective Diffusivity on the Flow Field. To investigate the effect of effective diffusivity (D_e) on the flow field, three effective diffusivities are selected, with their values being 1×10^{-11}, 5×10^{-11}, and 1×10^{-10} $m^2 \cdot s^{-1}$, respectively. The simulated results are shown in Figures 16–18.

Figures 16–18 give the contours of solid volume holdup distributions at different times when the values of D_e are 1×10^{-11}, 5×10^{-11}, and 1×10^{-10} $m^2 \cdot s^{-1}$, respectively. From Figure 16, the fluidization bed height increases as polymerization proceeds and small bubbles start to form in the bed at 1.0 s. In addition, the bed is completely fluidized after 1.6 s. From Figures 17 and 18, one can find that there are similar fluidization phenomena for the evolution of bed height when compared to Figure 16. However, bubble formation is not obvious in the bed after 1.0 s, while, the bed tends to fully fluidize at 1.6 s (see Figure 16). It does not achieve a complete fluidization at 1.6 s when the value of D_e reaches to 1×10^{-10} $m^2 \cdot s^{-1}$ (see Figure 18). Based on the PMLM, the intraparticle propylene concentration increases with the decrease of the internal mass transfer resistance and the intraparticle polymerization rate increases with the increase of the intraparticle propylene concentration, so that the particle growth rate increases with the increase of D_e. Furthermore, the gas–solid drag force of small particles is stronger than that of large particles, therefore one can conclude that it takes less time to arrive at the complete fluidization state and it is easier to form bubbles in the bed at the smaller value of D_e. Based on the above simulation results, it is realized that considering the effect of D_e on the flow field is important.

The Effect of Effective Thermal Conductivity on the Flow Field. To investigate the effect of effective thermal conductivity coefficient (K_e) on the flow field, three effective thermal conductivity coefficients are selected, namely, they are

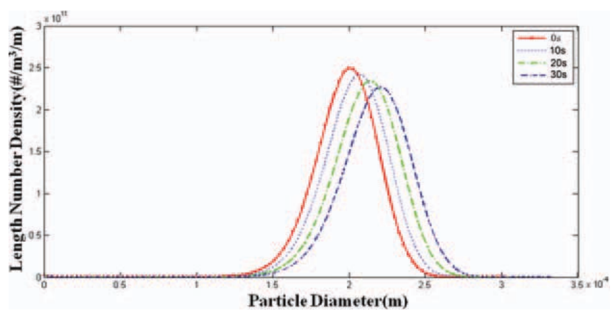

Figure 15. The evolution of PSD with time in Case 5.

[Color figure can be viewed in the online issue, which is available at wileyonlinelibrary.com.]

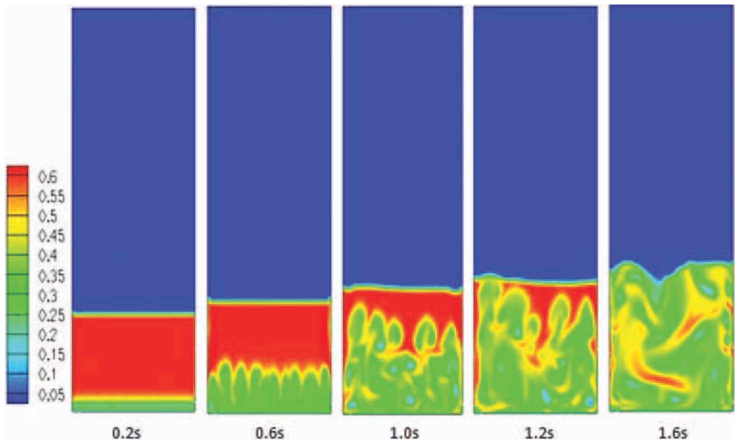

Figure 16. The evolution of solid volume fraction contour in the reactor ($D_e = 1 \times 10^{-11}$ m$^2 \cdot$ s^{-1}, $K_e = 0.18$ W·m^{-1} K^{-1}).

[Color figure can be viewed in the online issue, which is available at wileyonlinelibrary.com.]

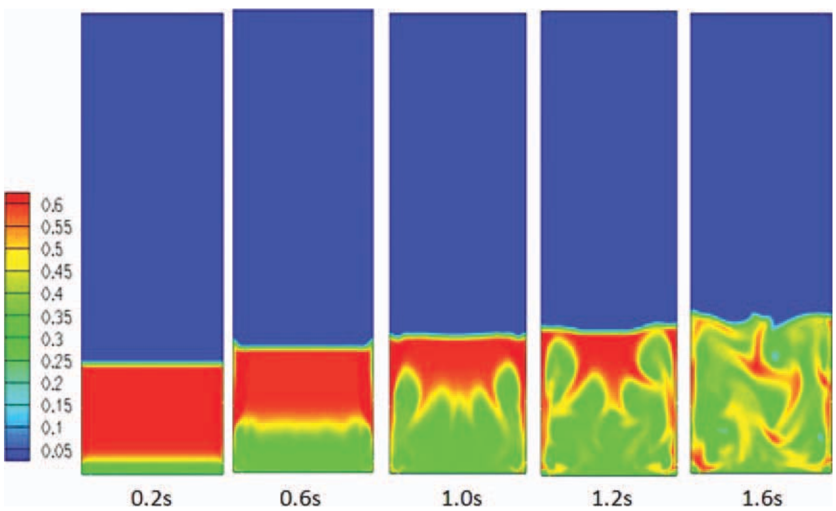

Figure 17. The evolution of solid volume fraction contour in the reactor ($D_e = 5 \times 10^{-11}$ m$^2 \cdot$ s^{-1}, $K_e = 0.18$ W·m^{-1} K^{-1}).

[Color figure can be viewed in the online issue, which is available at wileyonlinelibrary.com.]

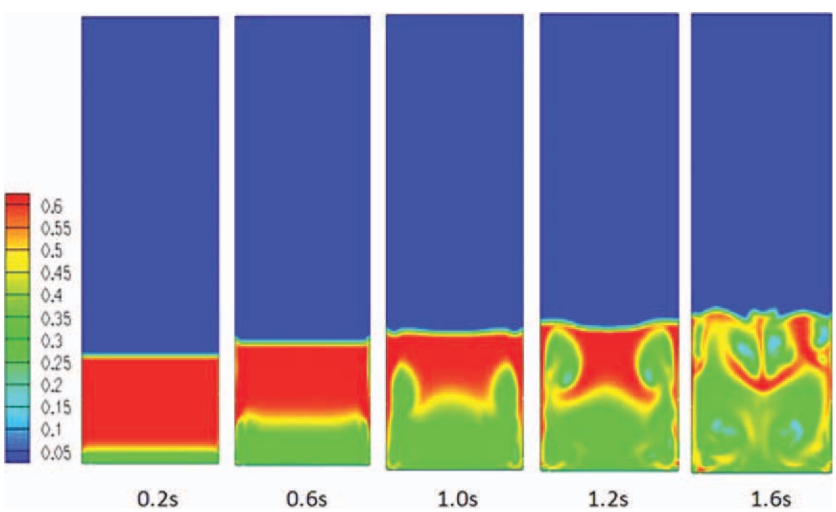

Figure 18. The evolution of solid volume fraction contour in the reactor ($D_e = 1 \times 10^{-10}$ m$^2 \cdot$ s^{-1}, $K_e = 0.18$ W·m^{-1} K^{-1}).

[Color figure can be viewed in the online issue, which is available at wileyonlinelibrary.com.]

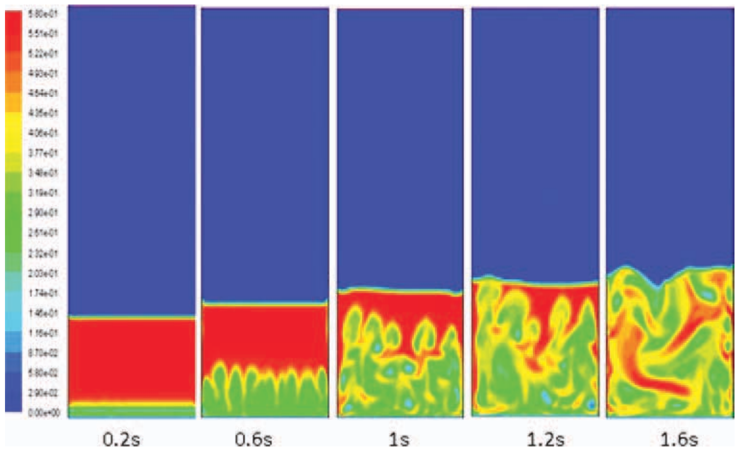

Figure 19. The evolution of solid volume fraction contour in the reactor (D_e = 1 × 10^{-11} $m^2 \cdot s^{-1}$, K_e = 0.12 W·m^{-1} K^{-1}).

[Color figure can be viewed in the online issue, which is available at wileyonlinelibrary.com.]

0.12, 0.16, and 0.18 W·m^{-1} K^{-1}, respectively. The value of D_e in these cases set to be 1 × 10^{-11} $m^2 \cdot s^{-1}$.

Figures 19 and 20 give the contours of solid volume holdup distributions at different times when the values of K_e are 0.12 W·m^{-1} K^{-1} and 0.16 W·m^{-1} K^{-1}, respectively. The contours of solid volume holdup at different times are shown in Figure 16 with K_e = 0.18 W·m^{-1} K^{-1}. From Figures 16, 19 and 20, one can find that the fluidization processes are nearly the same at the three conditions. With the increase of K_e, the maximum solid holdup increases from 0.58 to 0.6 at the full fluidization state. From the PMLM, it can be seen that the intraparticle polymerization rate increases with the increase of K_e. Accordingly, a larger K_e leads to larger average particle diameter at the same time spot when compared with the others, and the larger particles are easier to form a higher solid holdup. However, the effect of K_e on the flow field is not large.

Conclusions

In this study, an integrated CFD-PBM-PMLM model using an Eulerian-Eulerian two-fluid model was described for the gas–solid flow in fluidized bed polymerization reactors. The new model incorporates the kinetics theory of granular flow, the population balance equations, and a single particle growth model. The new model has been preliminarily validated by comparing simulation results with some classical experimental data. Also, five case studies: (i), with evolving fluid dynamics coupled purely continuous PSD; (ii), with pure particle growth; (iii), with pure particle aggregation; (iv), with pure particle breakage; and (v), with evolving flow dynamics coupled with all the above factors, were designed to put forward the comprehensive model. Finally, the most complete model was used to investigate the influences of intraparticle transfer limitations on the flow fields.

The simulated results show that the new model is appropriate to simulate the flow fields in the fluidized bed polymerization reactors. The fluidization process is complex due to the existence of complex collisions of particles including three types of particle kinetics factors, i.e., particle growth, aggregation, and breakage. On the other hand, the above particle kinetics factors are coupled with the PSD. Therefore, the PSD also changes during the progress of polymerization. The simulation results also show that the intraparticle mass transfer limitation is an important factor in affecting the reactor flow fields. With the increase of intraparticle mass transfer limitation, the fluidization time to reach the complete fluidization state decreases and the bubbles are easy to form in the reactor. Differently, the intraparticle heat transfer limitation does not affect much the reactor flow fields. The simulation results

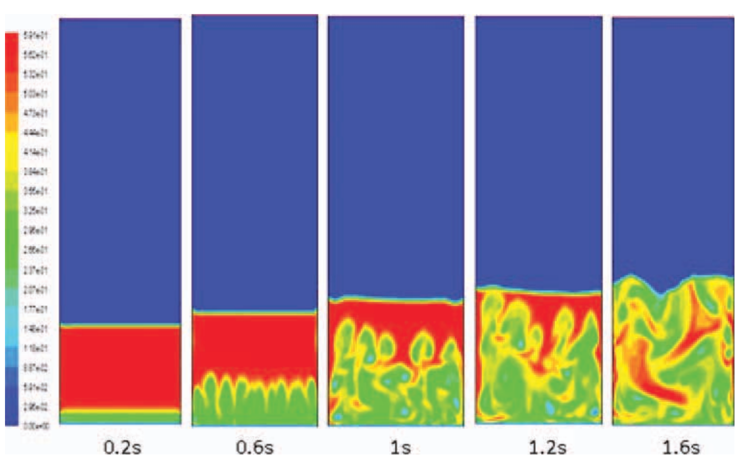

Figure 20. The evolution of solid volume fraction contour in the reactor (D_e = 1 × 10^{-11} $m^2 \cdot s^{-1}$, K_e = 0.16 W·m^{-1} K^{-1}).

[Color figure can be viewed in the online issue, which is available at wileyonlinelibrary.com.]

show that the fluidization processes are nearly the same at different intraparticle heat transfer limitations. Further studies on the integrated CFD-PBM-PMLM model for the gas–solid flow in FBR are in progress in the same research group.

Acknowledgments

The authors thank the National Natural Science Foundation of China (No. 21076171), the State-Key Laboratory of Chemical Engineering of Tsinghua University (No. SKL-ChE-10A03) and China National Petroleum Corporation for supporting this work. The authors also thank the anonymous referees for the comments on this manuscript.

The simulation work was implemented by advanced software tools (FLUENT 6.3.26 and GAMBIT 2.3.16) provided by China National Petroleum Corporation and its subsidiary companies.

Notation

$B_{ag,kk}$ = birth rate of particles due to aggregation (s^{-1})
$B_{br,kk}$ = birth rate of particles due to breakage (s^{-1})
C = catalyst concentration ($mol \cdot m^{-3}$)
C_μ, $C_{1\varepsilon}$, $C_{2\varepsilon}$ = coefficients in turbulence model
C_d = drag coefficient
C_p = heat capacity of the polymer particle ($J \cdot mol^{-1} \cdot K^{-1}$)
$C_{p,i}$ = heat capacity coefficient of the ith phase ($J \cdot mol^{-1} \cdot K^{-1}$)
$C_{p,s}$ = heat capacity of solid phase ($J \cdot mol^{-1} \cdot K^{-1}$)
C^* = active catalyst concentration ($mol \cdot m^{-3}$)
C_0^* = initial active site concentration ($mol \cdot m^{-3}$)
$D_{ag,kk}$ = death rate of particles due to aggregation (s^{-1})
$D_{br,kk}$ = death rate of particles due to breakage (s^{-1})
D_e = effective diffusivity ($m^2 \cdot s^{-1}$)
D_0 = initial catalyst radius (m)
e_i = particle–particle restitution coefficient
e_w = particle-wall restitution coefficient
E_A = activation energy of propylene polymerization ($J \cdot mol^{-1}$)
E_D = activation energy of catalyst deactivation reaction ($J \cdot mol^{-1}$)
g_0 = gravitational acceleration ($m \cdot s^{-2}$)
G = particle growth rate ($m \cdot s^{-1}$)
$G_{k,m}$ = production of turbulent kinetics energy ($kg \cdot m^{-1} \cdot s^{-3}$)
$\bar{\bar{I}}$ = identity matrix
k = turbulence kinetics energy tensor
k_d = catalyst deactivation rate constant (s^{-1})
k_0^d = frequency factor of catalyst deactivation reaction (s^{-1})
k_p = propagation rate related to the temperature of particle ($m^3 \cdot mol^{-1} \cdot s^{-1}$)
k_0^p = frequency factor of propagation reaction ($m^3 \cdot mol^{-1} \cdot s^{-1}$)
kk = specified number of moments
kk_1 = proportionality constants in Eq.(14)
kk_2 = proportionality constants in Eq.(14)
K_e = effective thermal conductivity of polymer particle ($W \cdot m^{-1} \cdot K^{-1}$)
KK = an aggregation rate constant which is a function of fluidizing temperature defined according to Eq. (14) ($m^{-6} \cdot s^{-1}$)
K_s = solid phase exchange coefficient ($kg \cdot m^2 \cdot s^{-1}$)
K_{gs} = interphase exchange coefficient ($kg \cdot m^2 \cdot s^{-1}$)
L, L_i, L_j, L_s = particle diameter (m)
L_0 = initial particle diameter (m)
L_{32} = the Sauter mean diameter (m)
$m_{g,inlet}$ = inlet gas flow ($kg \cdot m^{-3}$)
m_{kk} = the kkth moment of number density function (m^{kk})
$\dot{m}$, $\dot{m}_{sp}$ = mass transfer rate between the gas and solid phase
$\overline{m}_{g,inlet}$ = inlet gas flow change rate ($kg \cdot m^{-3} \cdot s^{-1}$)
M = monomer concentration ($mol \cdot m^{-3}$)
M_0 = bulk polypropylene concentration ($mol \cdot m^{-3}$)
M_m = molecular weight of propylene ($kg \cdot mol^{-1}$)
n = axial distance (m)
p = pressure (Pa)
p_s = particulate phase pressure (Pa)
q_i = heat flux ($W \cdot m^{-2}$)
Q_p, Q_{rs} = total polymerization heat of solid phase in reactor (W)
r = radial position in growing polymer particle (m)
R = radius of polymer particle (m)
R_{gas} = gas constant (= 8.314) ($J \cdot mol^{-1} \cdot K^{-1}$)
R_P = polymerization reaction rate ($mol \cdot m^{-3} \cdot s^{-1}$)
Re_s = Reynolds number of a particle
t = time (s)
T = temperature (K)
T_0 = temperature of bulk polymerization phase (K)
U_{mf} = minimum fluidization velocity ($m \cdot s^{-1}$)
U_t = particle terminal velocity ($m \cdot s^{-1}$)
$\vec{u}$ = particle growth rate vector due to processes other than interaction with other particles ($m \cdot s^{-1}$)
V = volume of polymer particle layer (m^3)
v_g = gas velocity ($m \cdot s^{-1}$)
$\vec{u}_m$ = velocity vector of system m ($m \cdot s^{-1}$)
v_s = solid velocity ($m \cdot s^{-1}$)
$v_{s,w}$ = solid velocity at wall ($m \cdot s^{-1}$)
w_i, w_j = mass fraction of particle i and j, respectively
x = spatial coordinate (m)
α_g = volume fraction of gas phase
α_i = volume fraction of phase i
α_s = volume fraction of solid phase
$\alpha_{s,m}$ = maximum volume fraction of solid phase
ε = turbulence dissipation rate ($m^2 \cdot s^{-3}$)
ϕ = specularity factor
μ_g = viscosity of gas phase (Pa·s)
μ_s = solid shear viscosity (Pa·s)
$\mu_{s,coi}$ = solid collisional viscosity (Pa·s)
$\mu_{s,kin}$ = solid kinetics viscosity (Pa·s)
$\mu_{s,fr}$ = solid frictional viscosity (Pa·s)
$\mu_{t,m}$ = frictional viscosity of system m (Pa·s)
σ_ε = granular kinetics theory parameter (kinetics viscosity) (Pa·s)
θ = angle of internal friction (deg)
Θ_s = granular temperature ($m^2 \cdot s^{-2}$)
γ_{Θ_s} = the collisional dissipation of energy ($m^2 \cdot s^{-2}$)
$\overline{\overline{\tau_g}}$ = shear stress of gas phase ($N \cdot m^{-2}$)
$\overline{\overline{\tau_S}}$ = shear stress of solid phase ($N \cdot m^{-2}$)
λ_s = solid bulk viscosity (Pa·s)
ρ_{cat} = catalyst density ($kg \cdot m^{-3}$)
ρ_g = gas density ($kg \cdot m^{-3}$)
ρ_i = density of phase i ($kg \cdot m^{-3}$)
ρ_m = density of system m ($kg \cdot m^{-3}$)
ρ_p = polymeric particle density ($kg \cdot m^{-3}$)
ρ_s = solid density ($kg \cdot m^{-3}$)
ΔH_p = heat of polymerization ($J \cdot mol^{-1}$)
$[R_p]$ = dimensionless polymerization rate
$[t]$ = dimensionless polymerization time

Literature Cited

1. Chai CJ, Zhang GL. *Chemical Engineering Fluid Flows and Heat Transport*. Beijing, China: Chemical Engineering Press (Chinese), 2004.
2. Yiannoulakis H, Yiagopoulos A, Kiparissides C. Recent developments in the particle size distribution modeling of fluidized-bed olefin polymerization reactors. *Chem Eng Sci*. 2001;56:917–925.
3. Khare NP, Seavey KC, Liu YA, Ramanathan S, Lingard S, Chen CC. Steady-state and dynamic modeling of commercial slurry high-density polyethylene (HDPE) processes. *Ind Eng Chem Res*. 2002; 41:5601–5618.
4. Khare NP, Luca B, Seavey KC, Liu YA. Steady-state and dynamic modeling of gas-phase polypropylene processes using stirred-bed reactors. *Ind Eng Chem Res*. 2004;43:884–900.
5. Luo ZH, Su PL, You XZ, Shi DP, Wu JC. Steady-state particle size distribution modeling of polypropylene produced in tubular loop reactors. *Chem Eng J*. 2009;146:466–476.
6. Zacca JJ, Debling JA, Ray WH. Reactor residence time distribution effects on the multistage polymerization of olefins - I. Basic principles and illustrative examples, polypropylene. *Chem Eng Sci*. 1996; 51:4859–4886.
7. Yogesh MH, Ranjeet PU, Vivek VR. A computational model for predicting particle size distribution and performance of fluidized bed polypropylene reactor. *Chem Eng Sci*. 2004;59:5145–5156.
8. Hatzantonis H, Goulas A, Kiparissides C. A comprehensive model for the prediction of particle-size distribution in catalyzed olefin polymerization fluidized-bed reactors. *Chem Eng Sci*. 1998;53:3251–3267.
9. McKenna TF. Spitz R, Cokljat D. Heat transfer from catalysts with computational fluid dynamics. *AIChE J*. 1999;45:2392–2410.
10. Cornelissen JT, Taghipour F, Escudié R, Ellis N, Grace JR. CFD modelling of a liquid-solid fluidized bed. *Chem Eng Sci*. 2007;62: 6334–6348.

11. Utikar RP, Ranade VV. Single jet fluidized beds: experiments and CFD simulations with glass and polypropylene particles. *Chem Eng Sci*. 2007;62:167–183.
12. Vaishali S, Roy S, Mills PL. Hydrodynamic simulation of gas-solids downflow reactors. *Chem Eng Sci*. 2008;63:5107–5119.
13. Cornelissen JT, Taghipour F, Escudié R, Ellis N, Grace JR. CFD modelling of a liquid-solid fluidized bed. *Chem Eng Sci*. 2007;62: 6334–6348.
14. Vaishali S, Roy S, Mills PL. Hydrodynamic simulation of gas-solids downflow reactors. *Chem Eng Sci*. 2008;63:5107–5119.
15. Darelius A, Rasmuson A, van Wachem B, Björn IN, Folestad S. CFD simulation of the high shear mixing process using kinetic theory of granular flow and frictional stress models. *Chem Eng Sci*. 2008;63:2188–2199.
16. Gao JS, Lan XY, Fan YP, Chang J, Wang G, Lu CX, Xu CM. CFD modeling and validation of the turbulent fluidized bed of FCC particles. *AIChE J*. 2009;55:1680–1694.
17. Min J, Drake JB, Heindel TJ, Fox RO. Experimental validation of CFD simulations of a lab-scale fluidized-bed reactor with and without side-gas. *AIChE J*. 2010;56:1434–1446.
18. Mahecha-Botero A, Grace JR, Elnashaie SSEH, Lim CJ. Advances in modeling of fluidized-bed catalytic reactors: a comprehensive review. *Chem Eng Comm*. 2009;196:1375–1405.
19. Shi DP, Luo ZH, Guo AY. Numerical simulation of the gas-solid flow in fluidized-bed polymerization reactors. *Ind Eng Chem Res*. 2010;49:4070–4079.
20. Wang HG, Yang WQ, Senior P, Raghavan RS, Duncan SR. Investigation of batch fluidized-bed drying by mathematical modeling, CFD simulation and ECT measurement. *AIChE J*. 2008;54:427–444.
21. Mohammad AD, Shahrokh S, Hashemabadi SH, Ghafelebashi SM. CFD based evaluation of polymer particles heat transfer coefficient in gas phase polymerization reactors. *Int Commun Heat Mass*. 2008; 35:1375–1379.
22. Busciglio A, Vella G, Micale G, Rizzuti L. Analysis of the bubbling behaviour of 2D gas solid fluidized beds Part II. Comparison between experiments and numerical simulations via digital image analysis technique. *Chem Eng J*. 2009;148:145–152.
23. Gidaspow D. *Multiphase Flow and Fluidization: Continuum and Kinetic Theory Descriptions*. Boston: Academic Press, 1994.
24. Cornelissen JT, Taghipour F, Escudié R, Escudié R, Grace JR. CFD modelling of a liquid-solid fluidized bed. *Chem Eng Sci*. 2007;62: 6334–6348.
25. Gao JS, Chang J, Lu CX, Xu CM. Experimental and computational studies on flow behavior of gas–solid fluidized bed with disparately sized binary particles. *Particuology*. 2008;6:59–71.
26. Sinclair JL. *Hydrodynamic Modeling in Circulating Fluidized Beds*. Blackie London: Academic and Professionals, 1997.
27. de Broqueville A, De Wilde J. Numerical investigation of gas-solid heat transfer in rotating fluidized beds in a static geometry. *Chem Eng Sci*. 2009;64:1232–1248.
28. Olmos E, Gentric C, Vial C, Wild G, Midoux N. Numerical simulation of multiphase flow in bubble column reactors: influence of bubble coalescence and breakup. *Chem Eng Sci*. 2001;56:6359–6365.
29. Lehr F, Mewes D. A transport equation for the interfacial area density applied to bubble columns. *Chem Eng Sci*. 2001;56:1159–1166.
30. Venneker BCH, Derksen JJ, van den Akker HEA. Population balance modeling of aerated stirred vessels based on CFD. *AIChE J*. 2002;48:673–685.
31. Buwa VV, Ranade VV. Dynamics of gas-liquid flow in a rectangular bubble column: experiments and single/multi-group CFD simulation. *Chem Eng Sci*. 2002;57:4715–4736.
32. Lo S. Application of population balance to CFD modeling of bubbly o/w via the MUSIG model. *AEA Technol*. 1996;AEAT-1096.
33. Fan R, Fox RO, Muhle ME. Role of intrinsic kinetics and catalyst particle size distribution in CFD simulation of polymerization reactors, In: *ECI Conference on the 12th International Conference on Fluidization-New Horizons in Fluidization Engineering*. Vancouver (Canada), 2007, pp 993–1000.
34. Fan R, Marchisio DL, Fox RO. Application of the direct method of moments to polydisperse gas-solid fluidized beds. *Powder Technol*. 2004;139:7–20.
35. Fan R. Computational Fluid Dynamics Simulation of Fluidized Bed Polymerization Reactors. Ph.D. Dissertation, Iowa State University, Iowa, 2006.
36. Fan R, Fox RO. Segregation in polydispersed fluidized beds: validation of a multi-fluid model. *Chem Eng Sci*. 2008;63:272–285.
37. Harshe YM, Utikar RP, Ranade VV. A computational model for predicting particle size distribution and performance of fluidized bed polypropylene reactor. *Chem Eng Sci*. 2004;59:5145–5156.
38. Luo ZH, Wen SH, Shi DP, Zheng ZW. Coupled single particle and population balance modeling for particle size distribution of polypropylene produced in loop reactors. *Macrom React Eng*. 2010;4:123–134.
39. Choi KY, Zhao X, Tang S. Population balance modeling for a continuous gas phase olefin polymerization reactor. *J Appl Polym Sci*. 1994;53:1589–1592.
40. Khang DY, Lee HH. Particle size distribution in fluidized beds for catalytic polymerization. *Chem Eng Sci*. 1997;52:421–431.
41. Sun GG, Grace JR. Effect of particle size distribution in different fluidization regimes. *AIChE J*. 1992;38:716–722.
42. Klett C, Hartge EU, Werther J. Time-dependent behavior of a catalyst in a fluidized bed/cyclone circulation system. *AIChE J*. 2007;53:769–779.
43. Alexopoulos AH, Roussos A, Kiparissides C. Part V: dynamic evolution of the multivariate particle size distribution undergoing combined particle growth and aggregation. *Chem Eng Sci*. 2009;64: 3260–3269.
44. Alexopoulos AH, Kiparissides C. On the prediction of internal particle morphology in suspension polymerization of vinyl chloride. Part I: the effect of primary particle size distribution. *Chem Eng Sci*. 2007;62:3970–3983.
45. Alexopoulos AH, Kiparissides C. Solution of the bivariate dynamic population balance equation in batch particulate systems: combined aggregation and breakage. *Chem Eng Sci*. 2007;62:5048–5053.
46. Meimaroglou D, Kiparissides C. Monte Carlo simulation for the solution of the bi-variate dynamic population balance equation in batch particulate systems. *Chem Eng Sci*. 2007;62:5295–5299.
47. Kanellopoulos V, Tsiliopoulou E, Dompazis G, Touloupides V, Kiparissides C. Evaluation of the internal particle morphology in catalytic gas-phase olefin polymerization reactors. *Ind Eng Chem Res*. 2007;46:1928–1937.
48. Mazzei L, Lettieri P, Marchisio DL. CFD simulations of the mixing of inert polydisperse fluidized suspensions using QMOM & DQMOM. In: *The 8th World Congress of Chemical Engineering*. Montréal (Canada). Canadian Society of Chemical Engineering, 2009:17–139.
49. Hulburt H, Katz S. Some problems in particle technology: a statistical mechanical formulation. *Chem Eng Sci*. 1964;19:555–574.
50. Ahmadzadeh A, Arastoopour H, Teymour F, Strumendo M. Population balance equations' application in rotating fluidized bed polymerization reactor. *Chem Eng Res Des*. 2008;86:329–343.
51. Rajniak P, Stepanek F, Dhanasekharan K, Fan R, Mancinelli C, Chern RT. A combined experimental and computational study of wet granulation in a Wurster fluid bed granulator. *Powder Technol*. 2009;189:190–201.
52. Balaji S, Du J, White CM, Ydstie BE. Multi-scale modeling and control of fluidized beds for the production of solar grade silicon. *Powder Technol*. 2010;199:23–31.
53. Moguel LF, Muhr H, Dietz A, Plasari E. CFD simulation of barium carbonate precipitation in a fluidized bed reactor. *Chem Eng Res Des*. 2010;88:1206–1216.
54. Chen XZ, Luo ZH, Yan WC, Lu YH, Ng IS. Three-dimensional CFD-PBM coupled model of the temperature fields in fluidized bed polymerization reactors. *AIChE J*. DOI:10.1002/aic.12548.
55. Luo ZH, Wen SH, Zheng ZW. Modeling the effect of polymerization rate on the intraparticle mass and heat transfer of propylene polymerization in a loop reactor, *J Chem Eng Jpn*. 2009;42:576–580.
56. Liu XG. Modeling and simulation of heterogeneous catalyzed propylene polymerization. *Chinese J Chem Eng*. 2007;15:545–553.
57. McKenna TF, Soares JBP. Single particle modelling for olefin polymerization on supported catalysts: a review and proposals for future developments. *Chem Eng Sci*. 2001;56:3931–3949.
58. Schmeal WR, Street JR. Polymerization in expanding catalyst particles. *AIChE J*. 1971;17:1189–1197.
59. Galvan R, Tirrell M. Orthogonal collocation applied to analysis of heterogeneous Ziegler–Natta polymerization. *Comput Chem Eng*. 1986;10:77–85.
60. Hutchinson RA, Chen CM, Ray WH. Polymerization of olefins through heterogeneous catalysis X: modeling of particle growth and morphology. *J Appl Polym Sci*. 1992;44:1389–1416.
61. Floyd S, Choi KY, Taylor TW, Tay WH. Polymerization of olefins through heterogeneous catalysis. IV. Modeling of heat and mass transfer resistance in the polymer particle boundary layer. *J Appl Polym Sci*. 1986;31:2231–2265.
62. Chen Y, Liu XG. Modeling mass transport of propylene polymerization on Ziegler–Natta catalyst. *Polymer* 2005;46:9434–9442.

63. Shi J, Liu XG. Melt index prediction by soft-sensor based on multi-scale analysis and principal component analysis. *Chinese J Chem Eng*. 2005;13:849–852.
64. Soares JBP, Hamielec AM. General dynamic mathematical modeling of heterogeneous Ziegler–Natta and metallocene catalyzed copolymerisation with multiple site types and mass and heat transfer resistance. *Polym React Eng*. 1995;3:261–324.
65. Soares JBP. Mathematical modelling of the microstructure of polyolefins made by coordination polymerization: a review. *Chem Eng Sci*. 2001;56:4131–4153.
66. Wang W, Zheng ZW, Luo ZH. Coupled-single-particle and Monte Carlo model for propylene polymerization. *J Appl Polym Sci*. 2011;119:352–362.
67. Syamlal M, Rogers W, O'Brien TJ. *MFIX Documentation: Volume 1, Theory Guide*. Springfield: National Technical Information Service, 1993.
68. Lun CKK, Savage SB, Jeffrey DJ, Chepurniy N. Kinetic theories for granular flow-inelastic particles in couette-flow and slightly inelastic particles in a general flow field. *J Fluid Mech*. 1984;140:223–232.
69. Ding J, Gidspow D. A bubbling fluidization model using kinetic-theory of granular flow. *AIChE J*. 1990;36:523–538.
70. Gunn DJ. Transfer of heat or mass to particles in fixed and fluidized beds. *Int J Heat Mass Transfer*. 1978;21:467–475.
71. Chen XZ, Shi DP, Gao X, Luo ZH. A fundamental CFD study of the gas-solid flow field in fluidized bed polymerization reactors. *Powder Technol*. 2011;205:276–288.
72. Bradshaw P, Cebeci T, Whitelaw JH. *Engineering calculation methods for turbulent flow*. London: Academic Press, 1981.
73. Chen CJ, Jaw SY. *Fundamentals of Turbulence Modeling*. Washington: Taylor & Francis, 1998.
74. Su JW, Gu ZL, Li Y, Feng SY, Xu XY. An adaptive direct quadrature method of moment for population balance equations. *AIChE J*. 2008;54:2872–2887.
75. Marchisio DL, Pikturan JT, Fox RO, Vigil RD, Barresi A. Quadrature method of moments for population-balance equations. *AIChE J*. 2003;49:1266–1276.
76. McGraw R. Description of aerosol dynamics by the quadrature method of moments. *Aerosol Sci Technol*. 1997;27:255–263.
77. Hatzantonis H, Goulas A, Kiparissides C. A comprehensive model for the prediction of particle-size distribution in catalyzed olefin polymerization fluidized-bed reactors. *Chem Eng Sci*. 1998;53:3251–3267.
78. Drumm C, Attarakih MM, Bart H. Coupling of CFD with DPBM for an RDC extractor. *Chem Eng Sci*. 2009;64:721–732.
79. Öncül AA, Niemann B, Sundmacher K, Thévenin D. CFD modelling of BaSO4 precipitation inside microemulsion droplets in a semi-batch reactor. *Chem Eng J*. 2008;138:498–509.
80. Baldyga J, Orciuch W. Closure problem for precipitation. *Chem Eng Res Des*. 1997;75:160–170.
81. Goldschmidt MJV. Hydrodynamic Modelling of Fluidised Bed Spray Granulation. Ph.D. Dissertation, Netherlands: Twente University, 2001.
82. Goldschmidt MJV, Link JM, Mellema S, Kuipers JAM. Digital image analysis measurements of bed expansion and segregation dynamics in dense gas-fluidised beds. *Powder Technol*. 2003;138:135–159.

Manuscript received Jan. 22, 2011, and revision received May 19, 2011.